



Measurement of Forward-Backward Asymmetry in $p\bar{p} \rightarrow t\bar{t}$ Production in the Dilepton Final States using a Matrix Element Technique

The DØ Collaboration

(Dated: October 1, 2014)

We present a measurement of the forward-backward asymmetry of $t\bar{t}$ production in dilepton final states, using 9.7 fb^{-1} of proton-antiproton collisions at $\sqrt{s} = 1.96 \text{ TeV}$ with the DØ detector. We select events with at least two jets, large missing transverse energy and two high momentum leptons, either two electrons, or two muons, or one muon and one electron. To reconstruct distributions of kinematic observables, we employ a matrix element technique that calculates the likelihood of the possible $t\bar{t}$ kinematic configurations. We then reconstruct the observable $A_{\text{FB}}^{t\bar{t}} = \frac{N(\Delta y_{t\bar{t}} > 0) - N(\Delta y_{t\bar{t}} < 0)}{N(\Delta y_{t\bar{t}} > 0) + N(\Delta y_{t\bar{t}} < 0)}$, where y_t ($y_{\bar{t}}$) is the top quark (antiquark) rapidity, $\Delta y_{t\bar{t}} = y_t - y_{\bar{t}}$, and N is a number of events. After accounting for the presence of background events and for calibration effects, the result interpreted as a test of the validity of the Standard Model is:

$$A_{\text{FB}}^{t\bar{t}} = (18.0 \pm 6.1(\text{stat}) \pm 3.2(\text{syst}))\%,$$

which is consistent with the Standard Model prediction of $A_{\text{FB}}^{t\bar{t}} = (8.8 \pm 0.6)\%$. Interpreted as a model independent measurement of the asymmetry, an additional uncertainty has to be accounted for due to the unknown top quark polarization, so that we obtain:

$$A_{\text{FB}}^{t\bar{t}} = (18.0 \pm 6.1(\text{stat}) \pm 3.2(\text{syst}) \pm 5.1(\text{model}))\%,$$

Preliminary Results for Autumn 2014

1. INTRODUCTION

In proton-antiproton collisions at $\sqrt{s}=1.96$ TeV, top quark pairs are predominantly produced via valence quark-antiquark annihilation. Within the Standard Model (SM), this process is predicted to be slightly forward-backward asymmetric: the top quark (antiquark) tends to be emitted in the same direction as the incoming quark (antiquark), and thus, in the same direction as the incoming proton (antiproton). The forward-backward asymmetry in the production is mainly due to positive contributions from the interferences between tree level diagrams and next-to-leading-order (NLO) box diagrams, but it receives smaller negative contributions from the interferences between initial state and final state radiations. In the SM, the asymmetry is predicted to be around 9% [1]. Physics beyond the SM could affect the $t\bar{t}$ production mechanism and thus its forward-backward asymmetry. In particular models with a new interaction violating parity, such as models with axiglons [2–5], can induce a large positive or negative asymmetry.

Several variables can be studied to assess the $t\bar{t}$ production asymmetry. For the decay $t \rightarrow W^+b \rightarrow \ell^+\nu b$ and $\bar{t} \rightarrow W^-b \rightarrow \ell^-\bar{\nu}b$, the charge q of the lepton indicates whether it comes from a top quark or antiquark, and we can use the lepton direction given by its pseudo-rapidity¹ (η) to build:

$$A_{\text{FB}}^\ell = \frac{N_\ell(q \times \eta > 0) - N_\ell(q \times \eta < 0)}{N_\ell(q \times \eta > 0) + N_\ell(q \times \eta < 0)}, \quad (1)$$

where $N_\ell(X)$ designates the number of leptons in configuration X . In the dilepton channel, one can also measure the difference in pseudo-rapidity of the leptons ($\Delta\eta = \eta_{\ell^+} - \eta_{\ell^-}$) to define:

$$A_{\text{FB}}^{\ell\ell} = \frac{N(\Delta\eta > 0) - N(\Delta\eta < 0)}{N(\Delta\eta > 0) + N(\Delta\eta < 0)}, \quad (2)$$

where $N(X)$ stands for the number of events in configuration X . Both A_{FB}^ℓ and $A_{\text{FB}}^{\ell\ell}$ are easy to reconstruct experimentally, however their values are the convolution of effects affecting both the $t\bar{t}$ production and also the top or anti-top decays.

A different observable can be defined using the difference, $\Delta y_{t\bar{t}} = y_t - y_{\bar{t}}$, between the rapidity² of the top quark, y_t , and the rapidity of the top antiquark, $y_{\bar{t}}$:

$$A_{\text{FB}}^{t\bar{t}} = \frac{N(\Delta y_{t\bar{t}} > 0) - N(\Delta y_{t\bar{t}} < 0)}{N(\Delta y_{t\bar{t}} > 0) + N(\Delta y_{t\bar{t}} < 0)}. \quad (3)$$

By definition this observable is independent of effects affecting top decay (*e.g.* top quark polarization). However, it is experimentally challenging to reconstruct the $t\bar{t}$ initial state from its decay products.

Measurements of $A_{\text{FB}}^{\ell\ell}$, A_{FB}^ℓ , and $A_{\text{FB}}^{t\bar{t}}$ have been performed by both DØ and CDF using both the dilepton final states, and the lepton+jets final states. They are summarized in Table 1, together with the SM expectations from Ref. [1]. Note that these three observables are predicted to have different values within the SM.

Source	Asymmetry in %		
	$A_{\text{FB}}^{\ell\ell}$	A_{FB}^ℓ	$A_{\text{FB}}^{t\bar{t}}$
SM prediction	4.8 ± 0.4 [1]	3.8 ± 0.3 [1]	8.8 ± 0.6 [1]
CDF lepton+jets	–	9.4 ± 3.0 [6]	16.4 ± 4.7 [7]
CDF dilepton	7.6 ± 8.2 [8]	7.2 ± 6.0 [8]	42 ± 16 [9]
DØ lepton+jets	–	5.0 ± 3.6 [10]	10.6 ± 3.0 [11]
DØ dilepton	12.3 ± 5.6 [12]	4.4 ± 3.9 [12]	This work

TABLE 1: Measurements of forward-backward asymmetry observables, performed at CDF and DØ, and comparison with the SM expectations.

This note presents the first measurement of $A_{\text{FB}}^{t\bar{t}}$ at DØ using Tevatron data in the dilepton channel. It is based on the full Run II (2002 – 2011) dataset of 9.7 fb^{-1} using $t\bar{t}$ final states with two leptons, either ee , $e\mu$, or $\mu\mu$. We first

¹ The pseudo-rapidity is defined as $\eta = -\ln(\tan \theta/2)$, where θ is the polar angle relative to the proton beam direction.

² The rapidity y is defined as $y = \frac{1}{2} \ln\left[\frac{(E+p_z)}{(E-p_z)}\right]$, where E is the particle energy and p_z is its momentum along the z -axis, which corresponds to the direction of the incoming proton.

reconstruct the $\Delta y_{t\bar{t}}$ distribution, employing an innovative modification of the matrix element integration technique used for the top-quark mass measurements at DØ [13, 14]. This distribution is used to extract a raw measurement of asymmetry, $A_{\text{raw}}^{t\bar{t}}$, in the data. Using a sample simulated with MC@NLO we compute the relation between the raw asymmetry $A_{\text{raw}}^{t\bar{t}}$ and the true parton-level asymmetry, $A_{\text{FB}}^{t\bar{t}}$, to determine calibration corrections. We then extract the final measured value of $A_{\text{FB}}^{t\bar{t}}$.

2. DETECTOR AND OBJECT RECONSTRUCTION

The DØ detector used for the Run II of the Tevatron collider is described in detail in Ref. [15–18]. The innermost part of the detector is composed of a central tracking system with a silicon microstrip tracker (SMT) and a central fiber tracker embedded within a 2 T solenoidal magnet. The tracking system is surrounded by a central preshower detector and a liquid-argon/uranium calorimeter with electromagnetic, fine, and coarse hadronic sections. The central calorimeter (CC) covers pseudorapidity $|\eta| \lesssim 1.1$. Two end calorimeters (EC) extend the coverage to $1.4 \lesssim |\eta| \lesssim 4.2$, while the coverage of the pseudorapidity gap where the ECs and CC overlap is augmented with scintillating tiles. A muon spectrometer, with pseudorapidity coverage of $|\eta| \lesssim 2$, is located outside the calorimetry and is comprised of drift tubes, scintillation counters, and toroidal magnets. Trigger decisions are based on information from the tracking detectors, calorimeters, and muon spectrometer.

Electrons are reconstructed as isolated clusters in the electromagnetic calorimeter, and required to spatially match a track in the central tracking system. They have to pass a Boosted Decision Tree (BDT) [19] criterion that accounts for calorimeter shower shape observables and isolation, a spatial track match probability estimate, and the ratio of the electron cluster energy to track momentum (E/p). Electrons are required to be in the acceptance of the electromagnetic calorimeter ($|\eta| < 1.1$ or $1.5 < |\eta| < 2.5$).

Muons are identified by the presence of at least one track segment reconstructed in the acceptance ($|\eta| < 2.0$) of the muon spectrometer, that is spatially consistent with a track in the central tracking detector [20]. The transverse momentum and charge are measured by the curvature in the central tracking system. To select isolated muons, the angular distance to the nearest jet, the momenta of central tracks emitted around the muon track, and the energy deposited around the muon trajectory in the calorimeter, are employed.

Jets are reconstructed from energy deposits in the calorimeter using an iterative midpoint cone algorithm [21] with a cone radius $\mathcal{R} = 0.5$ ³. The jet energies are calibrated using transverse momentum balance in γ +jet events [22].

3. DATASET AND EVENT SELECTION

The signature of $t\bar{t}$ production in the dilepton final states consists of two high p_T isolated leptons, two high p_T jets arising from the showering of two b -quarks, and missing transverse energy (\cancel{E}_T) due to the undetected neutrinos. We use the full DØ dataset consisting of 9.7 fb^{-1} of $p\bar{p}$ collision data. Our selection consists of three channels, ee , $e\mu$, and $\mu\mu$.

The main backgrounds in this final state arise from $Z \rightarrow \ell\ell$ and diboson production (WW , WZ , ZZ). These backgrounds are evaluated from Monte Carlo (MC) simulated samples as described in Sec. 4.3. Another source of background comes from W +jets and multijet events, when one or two jets are misreconstructed as an electron or when a muon from a jet passes the isolation criteria and is identified as a muon. The contributions from these backgrounds, denoted as “fake events”, are estimated directly from data as described in Sec. 4.4. Each of the dilepton channels is subject to a different mixture and level of background contamination, in particular for the background arising from Drell-Yan process. Therefore the three channels have slightly different selection criteria.

The selection is very similar to what was used for the measurement of A_{FB}^ℓ and $A_{\text{FB}}^{\ell\ell}$ [12], except that the final jet energy scale calibration of DØ is employed [22], and that both topological and b -tagging criteria (see below) have been re-optimized. The main selection criteria to obtain the final samples of $t\bar{t}$ candidate events are:

1. We select two high p_T ($p_T > 15 \text{ GeV}$) isolated leptons of opposite charge.
2. We require that at least one electron passes a single electron trigger condition in the ee channel (roughly 100% efficient), and that at least one muon passes a single muon trigger condition in the $\mu\mu$ channel (roughly 85% efficient). In the $e\mu$ channel we do not require any specific trigger condition (roughly 100% efficient).

³ Here, $\mathcal{R} = \sqrt{(\Delta\phi)^2 + (\Delta\eta)^2}$, where ϕ is the azimuthal angle around the proton beam direction.

3. We require the event to contain two or more jets of $p_T > 20$ GeV,
4. We further improve the purity of the selection by exploiting the significant imbalance of transverse energy due to undetected neutrinos and by exploiting the presence of several highly energetic objects due to the large top quark mass. To make use of these properties several topological observables are considered:
 - (a) The missing transverse energy, \cancel{E}_T , is the magnitude of the missing transverse momentum, obtained from the vector sum of the transverse components of energy deposits in the calorimeter, corrected for the differences in detector response of the reconstructed muons, electrons, and jets.
 - (b) The missing transverse energy significance, \cancel{E}_T^{sig} , is obtained as the logarithm of the probability to measure \cancel{E}_T in the hypothesis that the true missing transverse momentum was zero, accounting for the energy resolution of individual reconstructed objects and underlying energy [23].
 - (c) We define H_T as the scalar sum of transverse momenta of the leading lepton and the two leading jets:

$$H_T = p_T(\text{leading lepton}) + p_T(\text{leading jet}) + p_T(\text{next to leading jet}). \quad (4)$$

We employ these variables as follows: in the ee channel we require $\cancel{E}_T^{sig} \geq 5$, in the $e\mu$ we require $H_T > 110$ GeV, and in the $\mu\mu$ channel we require $\cancel{E}_T^{sig} \geq 5$ and $\cancel{E}_T > 40$ GeV.

5. For each of three channels we use a different cut on the multivariate discriminant described in Ref. [24] to demand that at least one of the two leading jets be b -tagged. The $t\bar{t}$ selection efficiency for this requirement is $\simeq 82\%$, $\simeq 83\%$, and $\simeq 75\%$, for respectively the ee , $e\mu$, and $\mu\mu$ channels.
6. The integration of the matrix elements by VEGAS, described in Sec. 5.1, may return a tiny probability which does not numerically allow the proper use of the event. We remove the events with low probability using a cut which has an efficiency at the level of 99.97% for $t\bar{t}$ MC. For background MC, the efficiency is higher than 99.3%. No event is removed from the final data sample by this cut.

4. SIGNAL AND BACKGROUND SAMPLES

4.1. DØ simulation

Signal and SM background processes except multijet and W +jets are simulated with the standard DØ simulation chain which consists of a detailed GEANT3-based [25] simulation of the DØ detector. In order to model the effects of multiple $p\bar{p}$ interactions, the Monte-Carlo (MC) events are overlaid with events from random $p\bar{p}$ collisions with the same luminosity distribution as data. Then, the MC events are processed with the same reconstruction software as used for the data. The jet energy calibration is adjusted in simulated events to match the one measured in data. Corrections for residual differences between data and simulation are applied to electrons, muons, and jets for both identification efficiencies and energy resolutions.

4.2. Signal

The selection presented in the previous sections is designed to select a relatively pure sample of $t\bar{t}$ events. To simulate this sample we employ MC events generated with MC@NLO 3.4 [26, 27] interfaced to HERWIG 6.510 [28] for showering and hadronization.

The events are generated with a top-quark mass of $m_t = 172.5$ GeV, using the CTEQ6M1 parton distribution functions (PDFs) [29]. They are normalized to a cross section of 7.45 pb which corresponds to the calculation of Ref. [30] for $m_t = 172.5$ GeV. The MC@NLO generator is used as it is supposed to simulate NLO effects yielding non-zero $A_{FB}^{t\bar{t}}$. The value of $A_{FB}^{t\bar{t}}$ measured in this sample using MC truth information without applying any selection requirement is $(5.23 \pm 0.07(\text{stat}))\%$.

4.3. Background estimated with simulated events

The $Z \rightarrow \ell\ell$ simulated events are generated using ALPGEN [31] interfaced to PYTHIA 6.4 [32] for showering and hadronization. This combination is denoted as ALPGEN+PYTHIA in the following.

We normalize the $Z \rightarrow \ell\ell$ sample to the NNLO cross section [33]. The p_T distribution of Z bosons is weighted to match the distribution observed in data [34], taking into account its dependence on the number of reconstructed jets.

The diboson backgrounds are simulated using PYTHIA and are normalized to the NLO cross section calculation performed by MCFM [35].

The background samples are generated using the CTEQ6L1 PDFs [29].

4.4. Background estimated with data: multijet and W +jets

The contributions from events with jets misidentified as electrons is estimated using the “matrix method” [36] separately for the ee and $e\mu$ channel. The contribution from jets producing identified muons in the $\mu\mu$ channel is obtained using the same selection criteria as for the samples of $t\bar{t}$ candidate events, but demanding that the leptons have the same charge. In the $e\mu$ channel it is obtained in the same way but after subtracting the contribution from events with jets misidentified as electrons.

The procedure described above aims at obtaining number of fake events. For the measurement of $A_{\text{FB}}^{t\bar{t}}$, “template samples” that mimic the kinematic of fake events are also needed. In the $e\mu$ channel, the template for fake events is obtained with the same selection criteria as for the samples of $t\bar{t}$ candidate events, but without applying the complete set of electron selection criteria. For the $\mu\mu$ and ee channels, the actual contributions from fake events is negligible, as reported in Table 2, so that the choice of template is unimportant. For simplicity, we re-employ the $e\mu$ template for both the $\mu\mu$ and ee channels.

4.5. DATA/MC comparison after selection

A comparisons between expected and observed numbers of events at the final selection levels is reported in Table 2.

	$Z \rightarrow \ell\ell$	Dibosons	Fake events	$t\bar{t} \rightarrow \ell\ell jj$, $\sigma_{t\bar{t}} = 7.454 \text{ pb}$ $m_t = 172 \text{ GeV}$	Expected N of events	N of events	$\frac{\text{Data}}{\text{MC}}$
$\mu\mu$ channel selection	$10.65^{+0.5}_{-0.5}$	$1.7^{+0.13}_{-0.13}$	$0.0^{+0.0}_{-0.0}$	$79.3^{+0.6}_{-0.6}$	$91.7^{+0.7}_{-0.7}$	92	1.00 ± 0.10
$e\mu$ channel selection	$13.03^{+0.5}_{-0.5}$	$3.7^{+0.2}_{-0.2}$	$16.4^{+0.7}_{-0.7}$	$283.1^{+1.0}_{-1.0}$	$316.2^{+1.3}_{-1.3}$	346	1.09 ± 0.05
ee channel selection	$12.92^{+0.4}_{-0.4}$	$1.9^{+0.1}_{-0.1}$	$1.8^{+0.08}_{-0.08}$	$95.5^{+0.6}_{-0.6}$	$112.1^{+0.8}_{-0.8}$	104	0.92 ± 0.10

TABLE 2: Comparison between expected and observed numbers of events at the final selection level for the different channels. The numbers are reported with their statistical uncertainties.

The comparison of distributions between actual data and expectations at the final selection level is shown in Fig .1.

5. MATRIX ELEMENT METHOD

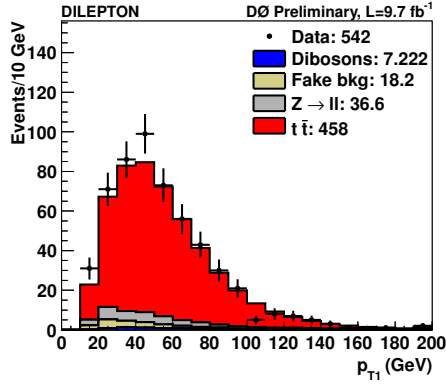
To reconstruct distributions of kinematic observables describing the $t\bar{t}$ events, we use an innovative modification of the matrix element (ME) integration performed for the top-quark mass measurements [13, 14] at DØ. In particular, this method is employed to reconstruct the $\Delta y_{t\bar{t}}$ distribution, from which an estimate of the forward-backward asymmetry is extracted.

5.1. Matrix element integration

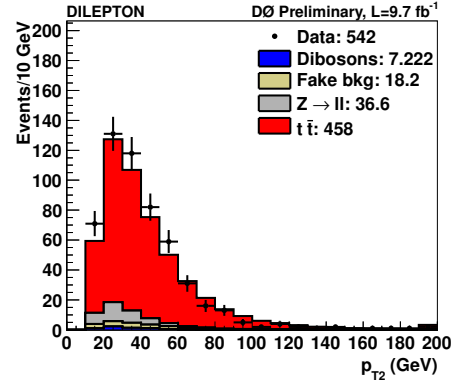
For a given event reconstructed with the vector of measured quantities z , we can compute a likelihood L_z to observe such an event:

$$L_z = \frac{1}{\mathcal{A} \cdot \sigma_{\text{tot}}} \sum_{\text{flavors}} \int_{x, q_1, q_2, p_T^{t\bar{t}}, \phi^{t\bar{t}}} W(x, z) W(p_T^{t\bar{t}}) f_{PDF}(q_1) f_{PDF}(q_2) \frac{(2\pi)^4 |\mathcal{M}|^2}{4\sqrt{(q_1 \cdot q_2)}^2} \cdot d\Phi_6 dp_T^{t\bar{t}} d\phi^{t\bar{t}} dq_1 dq_2. \quad (5)$$

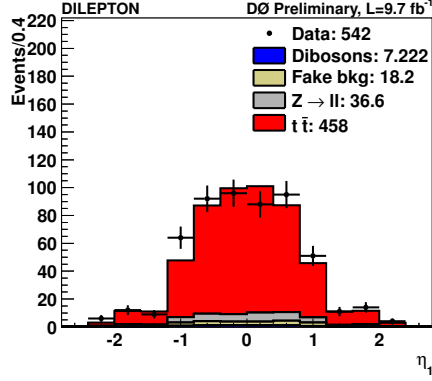
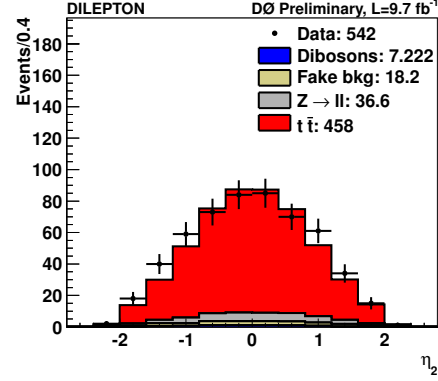
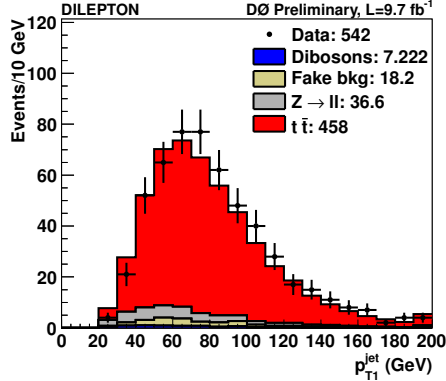
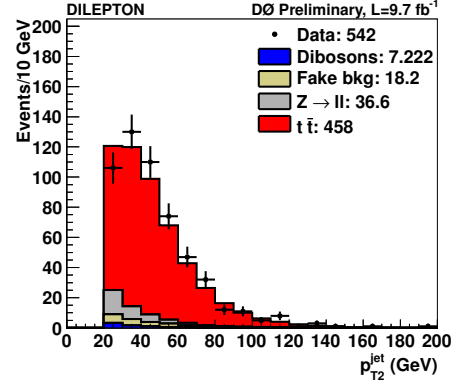
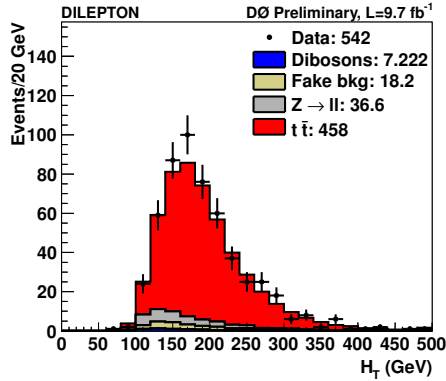
In this expression,



(a) Transverse momentum of the leading lepton.



(b) Transverse momentum of the secondary lepton.

(c) η of the leading lepton.(d) η of the secondary lepton.(e) p_T of the leading jet.(f) p_T of the secondary jet.

(g) Scalar sum of the leading lepton transverse momentum and the transverse momenta of two leading jets.

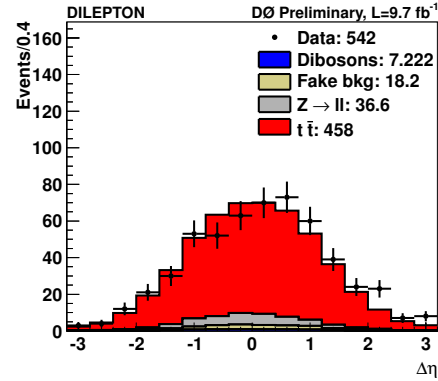
(h) $\Delta\eta$ between the two leptons.

FIG. 1: Comparison of distributions between data (points) and expectations (filled areas) at the final selection level for the dilepton events.

- x is a vector describing the kinematic quantities of the six particles of the $p\bar{p} \rightarrow t\bar{t} \rightarrow \ell^+\nu b \ell^-\bar{\nu}\bar{b}$ final state,
- z is the vector corresponding to measured quantities, \mathcal{M} is the matrix element describing the dynamics of the process,
- $d\Phi_6$ is the 6-body phase space term,
- the functions f_{PDF} are the PDFs of the incoming partons of 4-momenta q_1 and q_2 ,
- $W(x, z)$, referred to as *transfer function*, describes the probability density of a parton state x to be reconstructed as z ,
- $W(p_T^{t\bar{t}})$ is a function describing the distribution of the $t\bar{t}$ system transverse momentum, $p_T^{t\bar{t}}$, while the azimuthal angle of this system, $\phi^{t\bar{t}}$, is assumed to have a flat distribution over $[0, 2\pi]$,
- and $\mathcal{A} \cdot \sigma_{tot}$ is the experimental acceptance times total cross-section.

The matrix element, \mathcal{M} , is computed at leading order (LO) for $q\bar{q}$ annihilation only, as it represents the main subprocess ($\simeq 85\%$) of the total $t\bar{t}$ production. The functions f_{PDF} are given by the CTEQ6L1 leading order PDF set. The function $W(p_T^{t\bar{t}})$ is derived from parton-level simulated events generated with ALPGEN+PYTHIA. More details on this function can be found in Ref. [37]. The ambiguities between partons and reconstructed particles assignments are properly handled by defining an effective transfer function that sums over all the different assignments. As we consider only the two leading jets in the integration process, there are only two possibilities to assign a given jet to either the b or \bar{b} partons. This sum is thus limited to two terms.

The number of variables to integrate is a priori given by the six three-vectors of final state partons (of known mass), the $t\bar{t}$ transverse momentum and transverse direction, and the longitudinal momenta of the two incoming partons. These 22 integration variables are reduced by the following constraints: the lepton and b -quark directions are assumed to be perfectly measured (8 constraints), the energy-momentum between the initial state and the final state is conserved (4 constraints), the $\ell^+\nu$ and $\ell^-\bar{\nu}$ system have a mass of $m_W = 80.4$ GeV (2 constraints), and the $\ell^+\nu b$ and $\ell^-\bar{\nu}\bar{b}$ system have a mass of $m_t = 172.5$ GeV (2 constraints). For the muon and jet energies, transfer functions have to be accounted for. The transfer functions are the same as used in [14]. The electron momentum measurement has a precision of approximately 3%, which is much better than the muon momentum resolution of typically 10% and the jet momentum resolution of typically 20%. We thus consider that the electron momenta are perfectly measured. This gives one additional constraint in the $e\mu$ channel and two additional constraints in the ee channel. Thus, we integrate over 4, 5, and 6 variables in respectively, the ee , $e\mu$, and $\mu\mu$ channels. The integration variables are: *i*) $p_T^{t\bar{t}}$, *ii*) $\phi^{t\bar{t}}$, *iii*) energy of leading jet, *iv*) energy of sub-leading jet, *v,vi*) energy of the muon(s) (if applicable).

The integration is performed using the Monte Carlo (MC) based numerical integration program VEGAS [38, 39]. The interface to the VEGAS integration algorithm is provided by the GNU Scientific Library (GSL) [40]. The Monte Carlo integration consists in randomly sampling the space of integration variables, computing a weight for each of the random points that accounts for both the integrand and the elementary volume of the sampling space, and eventually summing all of the weights. The random sampling is based on a grid in the space of integration that is iteratively optimized to ensure fine sampling in regions with large variations of the integrand. For each of the random points, equations are solved to transform these integration variables into the parton-level variables of Eq. (5), accounting for the measured quantities z . The Jacobian of that transformation is also computed to assure proper weighting of the sampling space elementary volume.

5.2. Likelihood of a parton-level observable using matrix element integration

For any kinematic quantity K reconstructed from the parton momenta x , for example $K(x) = y_t - y_{\bar{t}}$, one can build a probability density $L_z(K)$ which measures the likelihood that $K(x)$ is equal to some value K given that we observed the reconstructed quantity z . This likelihood is obtained by inserting a $\delta(K(x) - K)$ in the integrand of expression (5), and by normalizing the function so that $\int L_z(K) dK = 1$. Technically, this quantity is obtained by slightly modifying the VEGAS integration algorithm. For a given reconstructed $t\bar{t}$ event, for each point in the integration space tested by VEGAS, the integrand of Eq. (5) is computed. For each of these points, we also compute the quantity K and store its value as well as the integration weight. After the integration, once the full space of integration has been sampled, we obtain a weighted distribution of the variable K which represents the function $L_z(K)$ up to an overall normalization factor.

For each reconstructed event z_i we obtain a likelihood function $L_{z_i}(K)$. By accumulating these likelihood functions over the sample of events, we obtain a distribution that estimates the true distribution of the variable K . The performance of this method of reconstruction for parton-level distributions can be estimated by comparing the accumulation of likelihood functions to the true parton-level quantities. Such a comparison is shown in Fig. 2.

5.3. DATA/MC comparison for distributions reconstructed with the matrix element integration

The ME reconstruction described above is applied in the dilepton data and in the simulated samples. Figure 3 shows a comparison of data and MC for the accumulation of likelihood functions $L_{z_i}(K)$ testing different quantities K . In particular Fig 3d shows the $\Delta y_{t\bar{t}}$ distributions.

5.4. Raw estimate of $A_{\text{FB}}^{t\bar{t}}$ using matrix element method

We could make the choice to use the maximum of the likelihood function $L_z(\Delta y_{t\bar{t}})$ to estimate the true value of $\Delta y_{t\bar{t}}$ on an event-by-event basis. However, to maximize the use of available information, we keep the full shape of $L_z(\Delta y_{t\bar{t}})$, and accumulate these functions over the sample of $t\bar{t}$ events to obtain an estimate of the parton level distribution of $\Delta y_{t\bar{t}}$, which can be used to compute $A_{\text{FB}}^{t\bar{t}}$. This method has been verified to be more sensitive than the maximum likelihood method.

For N_{events} events, the accumulation of likelihood functions reads:

$$L(\Delta y_{t\bar{t}}) = \sum_{i=1}^{N_{\text{events}}} L_{z_i}(\Delta y_{t\bar{t}}), \quad (6)$$

and we can define a raw asymmetry, $A_{\text{raw}}^{t\bar{t}}$, as the relative difference between the positive and negative part of this distribution:

$$A_{\text{raw}}^{t\bar{t}} = \frac{\int_0^\infty L(\Delta y_{t\bar{t}}) - \int_{-\infty}^0 L(\Delta y_{t\bar{t}})}{\int_0^\infty L(\Delta y_{t\bar{t}}) + \int_{-\infty}^0 L(\Delta y_{t\bar{t}})} \quad (7)$$

It should be noticed that Eq.(7) can be expanded as:

$$A_{\text{raw}}^{t\bar{t}} = \frac{\sum_{i=1}^{N_{\text{events}}} \left[\int_0^\infty L_{z_i}(\Delta y_{t\bar{t}}) - \int_{-\infty}^0 L_{z_i}(\Delta y_{t\bar{t}}) \right]}{\sum_{i=1}^{N_{\text{events}}} 1} \quad (8)$$

$$= \frac{1}{N_{\text{events}}} \sum_{i=1}^{N_{\text{events}}} A_i, \quad (9)$$

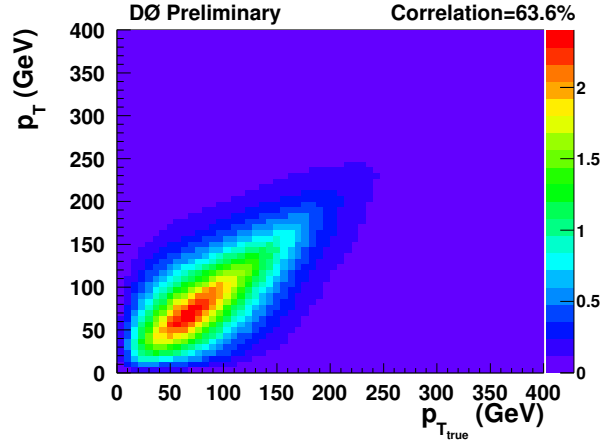
so that the raw asymmetry is the average, over the sample of $t\bar{t}$ candidate events, of the variable A , defined as the event-by-event asymmetry of the likelihood function $L_z(\Delta y_{t\bar{t}})$:

$$A_i = \int_0^\infty L_{z_i}(\Delta y_{t\bar{t}}) - \int_{-\infty}^0 L_{z_i}(\Delta y_{t\bar{t}}). \quad (10)$$

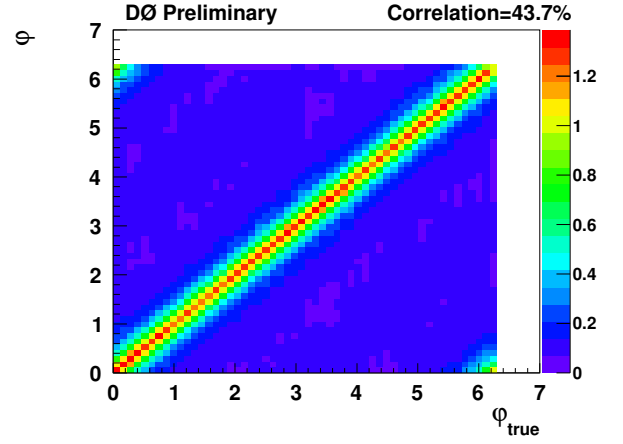
By construction (*i.e.*, given that $\int L_z(\Delta y_{t\bar{t}}) = 1$), the variable A is in the interval $[-1, +1]$. For a perfect reconstruction without resolution effect, A would be either equal to -1 or to $+1$, indicating whether $\Delta y_{t\bar{t}}$ were respectively negative or positive.

In our analysis we use the distributions of A for two main reasons:

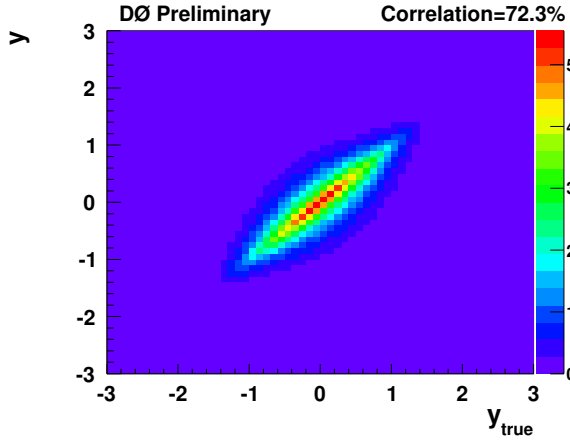
1. Technically it is more convenient to handle an event-by-event variable, rather than an event-by-event function or histogram.
2. Equation (9) demonstrates that the statistical uncertainty on $A_{\text{raw}}^{t\bar{t}}$ is the uncertainty on the average value of A , which can be estimated in a straightforward way.



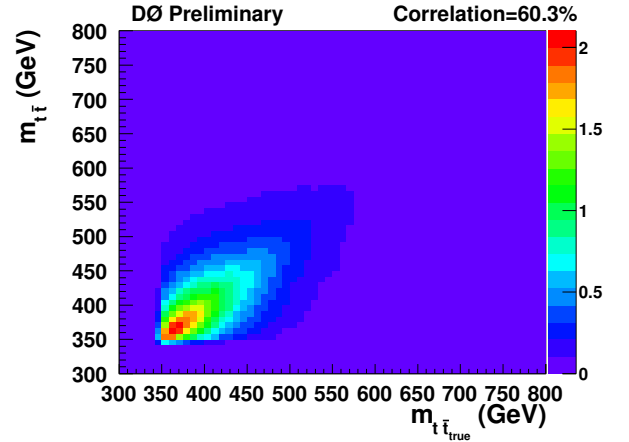
(a) $\sum_{events} L_{z_i}(p_T)$ vs $p_{T,true}$ for the p_T of the top quark or anti-quark.



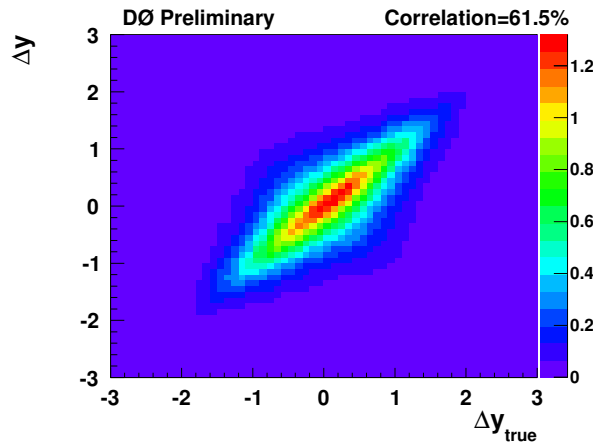
(b) $\sum_{events} L_{z_i}(\phi)$ vs ϕ_{true} for the azimuthal angle ϕ of the top quark or anti-quark.



(c) $\sum_{events} L_{z_i}(y_t)$ vs $y_{t,true}$ for the rapidity of the top quark or anti-quark.



(d) $\sum_{events} L_{z_i}(M_{t\bar{t}})$ vs $M_{t\bar{t},true}$.



(e) $\sum_{events} L_{z_i}(\Delta y_{t\bar{t}})$ vs $\Delta y_{t\bar{t},true}$.

FIG. 2: Accumulation of likelihood functions ($\sum_{events} L_{z_i}(K)$, with K along the Y-axis) vs corresponding true parton level quantity (K_{true} along the X-axis) from $t\bar{t}$ MC events for the $e\mu$ channel after selection cuts. Each single MC event i contributes in these plots with a complete distribution, $L_{z_i}(K)$, along the Y-axis for a fixed X-axis position, K_{true} .

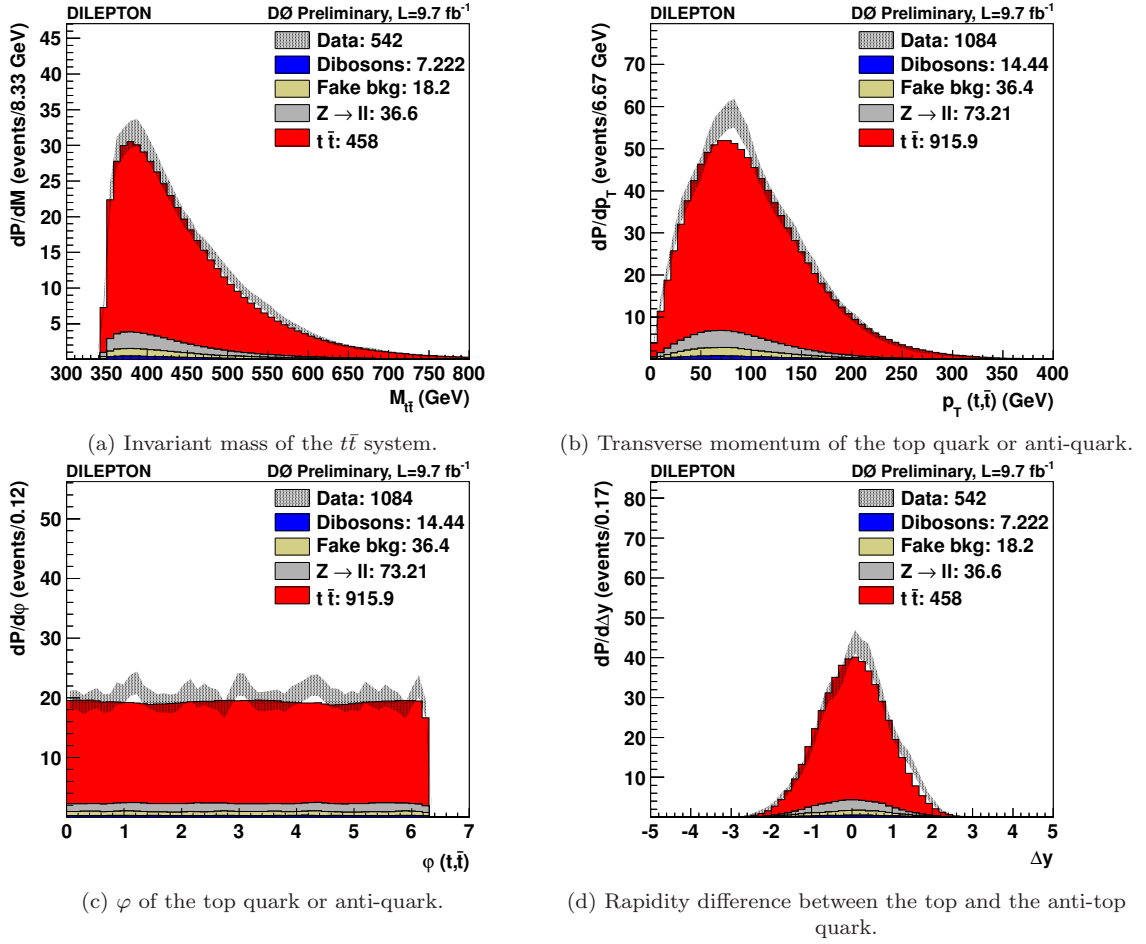


FIG. 3: For the combination of dilepton channels, comparison of distributions between data (band) and expectations (filled areas) after reconstructing the $t\bar{t}$ system kinematics. Each single data event i corresponds to a likelihood function $L_{z_i}(K)$ for the quantity K . The statistical uncertainty for the accumulation of data events is represented by the cross-hatched uncertainty band.

The distribution of $\sum_{events} L_{z_i}(\Delta y_{t\bar{t}})$ and the distribution of A are shown in Fig. 4 for data and simulation after subtracting the background distributions. The raw asymmetry, $A_{raw}^{t\bar{t}}$, is extracted from either of these distributions. The result is reported in Table 3 where it is broken down into the contributions of signal and background for the different dilepton channels.

The distribution $\frac{1}{N_{events}} \sum_{events} L_{z_i}(\Delta y_{t\bar{t}})$ is an approximate estimate of the true distributions of $\Delta y_{t\bar{t}}$, so that the raw asymmetry, $A_{raw}^{t\bar{t}}$, is also an approximate estimate of the true $A_{FB}^{t\bar{t}}$. The measurement needs therefore to be calibrated as described in the next section.

channel	A_{raw}^{data}	A_{raw}^{bkg}	$A_{raw}^{t\bar{t}}$
$e\mu$	0.092 ± 0.038 (stat)	0.003 ± 0.018 (stat)	0.101 ± 0.042 (stat)
ee	0.158 ± 0.064 (stat)	0.001 ± 0.020 (stat)	0.188 ± 0.076 (stat)
$\mu\mu$	0.067 ± 0.079 (stat)	-0.003 ± 0.033 (stat)	0.078 ± 0.091 (stat)
dilepton	0.100 ± 0.030 (stat)	0.001 ± 0.012 (stat)	0.113 ± 0.034 (stat.)

TABLE 3: For the different dileptonic channels, raw asymmetry measurement in the data before background subtraction, A_{raw}^{data} , asymmetry of the background, A_{raw}^{bkg} , and measurement once the background contribution has been subtracted, $A_{raw}^{t\bar{t}}$. The combined result is obtained by considering the accumulation of the distributions from the three dilepton channels.

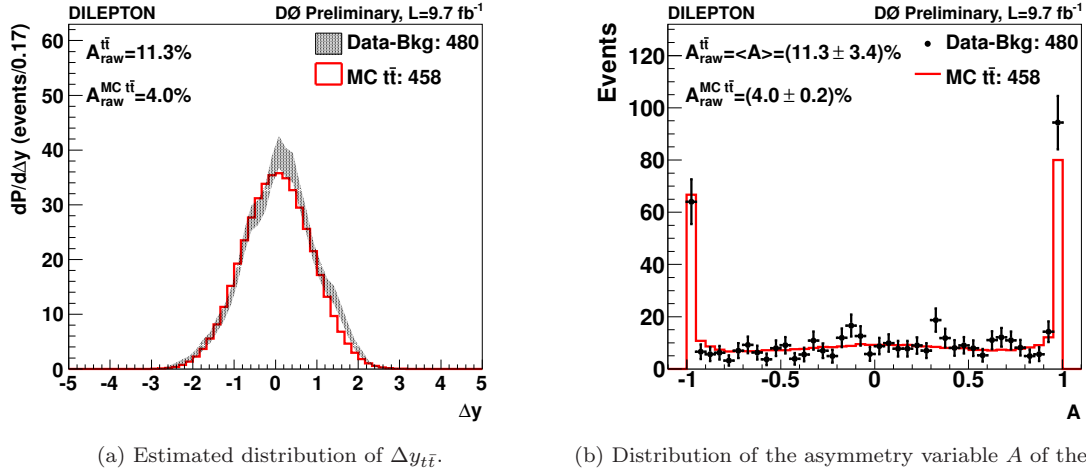


FIG. 4: Estimate of the $\Delta y_{t\bar{t}}$ distribution and distribution of A , obtained after combining the three dilepton channels and subtracting the background distributions.

6. RESULTS CORRECTED FOR CALIBRATION

The calibration consists of finding a relation between the raw asymmetry $A_{\text{raw}}^{t\bar{t}}$, obtained after subtracting the background contributions, and the true asymmetry $A_{\text{FB}}^{t\bar{t}}$ of $t\bar{t}$ events. The need for calibration is due to dilution effects that arise from the limited $t\bar{t}$ acceptance, the finite resolution of the kinematic reconstruction, and the simplified assumption used in the matrix element integration (*e.g.* leading order ME, no $gg \rightarrow t\bar{t}$ ME, only 2 jets considered). The relation is then inverted to extract a measurement of $A_{\text{FB}}^{t\bar{t}}$ from the value of $A_{\text{raw}}^{t\bar{t}}$ observed in the data.

The calibration is determined using a sample of simulated $t\bar{t}$ MC@NLO dilepton events. We choose to normalize the individual ee , $e\mu$ and $\mu\mu$ contributions to have the same proportions as observed in the data samples after subtracting the expected background contributions. Since the calibration constants are the same at the 2% level in the three channels, and since the normalization factors are close to unity at the 15% level, this choice yields the same final $A_{\text{FB}}^{t\bar{t}}$ measurement as if we had chosen to use the expected proportions.

6.1. Calibration

Starting from a single MC@NLO sample, we produce pseudo-samples of different partonic-level $A_{\text{FB}}^{t\bar{t}}$. The pseudo-samples are obtained by reweighting the MC@NLO events according to a function of the true $\Delta y_{t\bar{t}}$ value. We employ a hyperbolic tangent function for the definition of the weights w :

$$w(\Delta y_{t\bar{t}}) = 1 + \beta \tanh\left(\frac{\Delta y_{t\bar{t}}}{\alpha}\right), \quad (11)$$

with α a shape parameter and β a magnitude parameter. This hyperbolic tangent form and the possible values of (α, β) are inspired by a study performed on various generators, simulating $t\bar{t}$ production within the Standard Model and within physics beyond the Standard Model [41].

$\beta \setminus \alpha$	0.5	1.1
-0.3	-0.161	-0.091
-0.1	-0.019	0.004
0.1	0.121	0.098
0.3	0.258	0.191

TABLE 4: Partonic-level $A_{\text{FB}}^{t\bar{t}}$ of the pseudo-samples as a function of the values of the shape parameter (α) and magnitude parameter (β) of the reweighting function.

6.2. Results of the calibration

To obtain the calibration curve we use 8 sets of parameters reported in Table 4 plus the non-reweighted MC@NLO sample. A systematic uncertainty associated to the choice of parameters is discussed in Sec. 7. For the 9 pseudo-samples, we apply the method of ME reconstruction and compare the raw measurement to the true partonic-level asymmetry. The results are shown on Fig. 5. The set of points are fitted with an affine function called the calibration curve. The calibration curve is characterized by slope coefficient ϵ_{calib} and an offset coefficient x_0 . As the MC@NLO pseudo-samples are not statistically independent, we use an ensemble method to properly estimate the statistical uncertainty on these parameters. We randomly split the MC@NLO samples into 100 independent ensembles and repeat the calibration procedure for each of the ensembles. The RMS of the calibration coefficients scaled by $1/\sqrt{100}$ is an estimate of the statistical uncertainty of the calibration coefficients. The calibration coefficients are reported in Table 5 together with their uncertainties as obtained by the ensemble method. We also report the calibration coefficients for the individual channels.

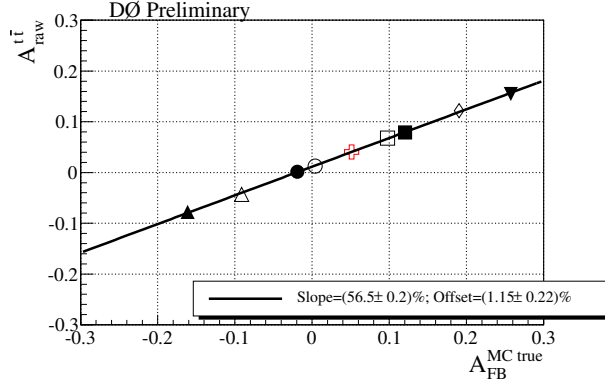


FIG. 5: Reconstructed raw asymmetry as a function of the true partonic asymmetry using pseudo-samples obtained from the default MC@NLO simulation. The different markers correspond to the different pseudo-samples (the red marker corresponds to the default MC@NLO sample). The calibration curves is fitted with an affine function.

channel	ϵ_{calib}	x_0
$e\mu$	0.566 ± 0.002	0.013 ± 0.002
ee	0.554 ± 0.003	0.009 ± 0.003
$\mu\mu$	0.574 ± 0.003	0.009 ± 0.004
dilepton	0.565 ± 0.002	0.011 ± 0.002

TABLE 5: Slope, ϵ_{calib} and offset, x_0 , coefficients obtained from the calibration for each channel and for the overall dilepton selection.

Note that we do not expect our method to yield a calibration with a slope close to 1. The variable $A_{\text{raw}}^{t\bar{t}}$ is actually not supposed to be an unbiased estimate of $A_{\text{FB}}^{t\bar{t}}$, but rather an observable correlated to $A_{\text{FB}}^{t\bar{t}}$. A simple toy-model assuming a Gaussian distribution for the true parton-level $\Delta y_{t\bar{t}}$ variable predicts a value of the slope parameter close to 0.5 because of the finite resolution of the $\Delta y_{t\bar{t}}$ reconstruction.

6.3. Measurement of $A_{\text{FB}}^{t\bar{t}}$ accounting for the calibration

The calibration coefficients obtained above are used to retrieve the true partonic asymmetry $A_{\text{FB}}^{t\bar{t}}$ from the reconstructed $A_{\text{raw}}^{t\bar{t}}$ with the formula:

$$A_{\text{FB}}^{t\bar{t}} = \frac{A_{\text{raw}}^{t\bar{t}} - x_0}{\epsilon_{\text{calib}}}. \quad (12)$$

We apply this formula to the $A_{\text{raw}}^{t\bar{t}}$ measurements reported in Table 3, and the calibration coefficients of Table 5. We obtain a measurement of $A_{\text{FB}}^{t\bar{t}}$ for each dileptonic channel reported in Table 6.

channel	$A_{\text{FB}}^{t\bar{t}}$
$e\mu$	0.156 ± 0.075 (stat.)
ee	0.323 ± 0.137 (stat.)
$\mu\mu$	0.122 ± 0.159 (stat.)
dilepton	0.180 ± 0.061 (stat.)

TABLE 6: $A_{\text{FB}}^{t\bar{t}}$ measurements for each dileptonic channel, after calibration.

7. SYSTEMATIC UNCERTAINTIES

We consider two kinds of uncertainties. Uncertainties affecting the signal have a direct impact on the calibration curve. These uncertainties are propagated to the final result by re-deriving $A_{\text{FB}}^{t\bar{t}}$ using modified calibration coefficients. Since the measurement is performed after background subtraction, the calibration is independent of the normalization of the $t\bar{t}$ simulation, and there is no systematic uncertainty due to signal normalization. Uncertainties affecting the background have an impact on the raw asymmetry, $A_{\text{raw}}^{t\bar{t}}$, which is obtained after subtracting the background. These uncertainties are propagated to the final measurement by applying the nominal calibration correction to the modified $A_{\text{raw}}^{t\bar{t}}$.

Several sources of systematic uncertainties due to the detector and reconstruction model affect the jets and thus the signal kinematics. We consider uncertainties on the jet energy scale, flavor-dependent jet response, and jet energy resolution [22]. We also consider uncertainties associated with b -tagging and vertexing [24].

The signal modeling uncertainty is derived from different sources. To propagate uncertainty on the simulation of initial state and final state radiations (ISR/FSR), the amount of radiation is varied by scaling the `ktfac` parameter either by 1.5 or by 1/1.5 in an ALPGEN+PYTHIA simulation of $t\bar{t}$ events [14]. The ISR/FSR uncertainty is determined by comparing the calibration curves obtained with these modified `ktfac` to what is obtained with the nominal ALPGEN+PYTHIA generator. The hadronization and parton-shower model uncertainty is derived from the difference between the PYTHIA and HERWIG generators, estimated by comparing ALPGEN+HERWIG to ALPGEN+PYTHIA $t\bar{t}$ samples. The different models for parton showers used by various MC generators yield different amounts of ISR between forward and backward events [42, 43]. We therefore account for an uncertainty on the model of difference of ISR between forward and backward events in our MC. It is obtained by reducing the difference in the distribution of the p_T of the $t\bar{t}$ system between forward and backward events down to 50% of the nominal difference. To estimate the impact of higher order correction, we compare the calibration obtained with MC@NLO+HERWIG to what is obtained with ALPGEN+HERWIG. We determine PDF uncertainties by varying within their uncertainty the 20 parameters describing the CTEQ6M1 PDF [29].

The uncertainty on the background level is conservatively obtained by varying the fake background normalization by 50%, and varying the overall background normalization by 20%. The model of the fake background kinematics is varied, using the same method as in Ref. [12]: we reweight each bin of the $\Delta y_{t\bar{t}}$ distribution by its associated uncertainty. The weights are chosen to be positive for $\Delta y_{t\bar{t}} > 0$ and negative for $\Delta y_{t\bar{t}} < 0$ to simulate an extreme variation of the shape of the distribution. As a consequence, the fake background asymmetry is shifted from $\simeq +2\%$ to $\simeq +10\%$ and this modification of shape is propagated to the final result.

We also consider sources of uncertainties affecting the calibration procedure. The statistical uncertainty on the fit parameters of the affine function used for calibration and their correlation are propagated to the final $A_{\text{FB}}^{t\bar{t}}$ measurement, giving a 0.4% uncertainty. The reweighting functions discussed in Sec. 6.1 are used to produce samples of various parton-level $A_{\text{FB}}^{t\bar{t}}$. To estimate a systematic uncertainty due to the choice of functional form, we test calibration correction obtain from using two extreme values of the shape parameter, $\alpha = 0$ and $\alpha = 10$, corresponding to two extreme behaviors of the tanh function. $\alpha = 0$ corresponds to a step-function, *i.e.*, the most non-linear behavior, while $\alpha = 10$ corresponds to a linear behavior, since $10 \gg 2.5$, where $[-2.5, 2.5]$ represents the spread of the $\Delta y_{t\bar{t}}$ distribution in MC. To test a method different from the reweighting based on hyperbolic tangent functions, we also conduct a calibration using pseudo-samples obtained by translating the $\Delta y_{t\bar{t}}$ distribution of the nominal MC. We report the maximum variation (2.7%) of the measured $A_{\text{FB}}^{t\bar{t}}$ obtained from these various tests as a systematic uncertainty.

The absolute variations on $A_{\text{FB}}^{t\bar{t}}$ due to the different sources of systematic uncertainties are summarized in Table 7.

Source of uncertainty	Uncertainty on $A_{\text{FB}}^{t\bar{t}}$ (%)
<i>Detector modeling</i>	
jet energy scale	0.14
jet energy resolution	0.17
flavor-dependent jet response	0.03
b -tagging	0.11
<i>Signal modeling</i>	
ISR/FSR	0.32
forward/backward ISR	0.36
hadronisation and showering	1.08
higher order correction	0.80
PDF	0.60
<i>Background model</i>	
fake background normalization	0.35
fake background shape	0.35
background normalization	0.53
<i>Calibration</i>	
$\Delta y_{t\bar{t}}$ model	2.7
calibration statistics	0.4
Total	3.2

TABLE 7: Summary of systematic uncertainties.

7.1. Closure tests using models beyond the Standard Model

One of the goals of $A_{\text{FB}}^{t\bar{t}}$ measurement is probing the consistency of the SM and probing physics beyond the SM (BSM). In this section we study the outcome of our method when applied on BSM models.

7.1.1. BSM benchmark models

We test the six BSM benchmark models discussed in Ref. [44]. Those models include axigluons [2, 5] or Z' gauge bosons [45]. For each of these models we process a $t\bar{t}$ sample, produced with the MADGRAPH [46] generator interfaced to PYTHIA for hadronization and showering, through the full DØ simulation chain. These benchmark models can be divided in three classes:

1. Light axigluons models: a light axigluon (i. e. $100 < m_G < 400$ GeV) yields a positive $t\bar{t}$ asymmetry. The decay width is chosen to be 50 GeV. We have generated three different models, differing by their right-handed and left-handed coupling constants to quarks i , $g_{R,i}$ and $g_{L,i}$, expressed in units of the strong coupling constant g_S .
 - (a) axigluon m200R5: $m_G = 200$ GeV, $\Gamma_G = 50$ GeV, $g_{R,i} = 0.5g_S$, $g_{L,i} = 0$
 - (b) axigluon m200L5: $m_G = 200$ GeV, $\Gamma_G = 50$ GeV, $g_{R,i} = 0$, $g_{L,i} = 0.5g_S$
 - (c) axigluon m200A4: $m_G = 200$ GeV, $\Gamma_G = 50$ GeV, $g_{R,i} = 0.4g_S$, $g_{L,i} = -0.4g_S$
2. Heavy axigluons models: A heavy axigluon leads to positive asymmetry only if the signs of the coupling constant to heavy quarks ($g_{R,t}$) and light quarks ($g_{R,u}$) are opposite. These particles are too heavy to be produced at the Tevatron. Thus, the decay width of these particles needs to be large to yield observable effects at the Tevatron energies. We have generated two samples of events:
 - (a) axigluon m2000w960: $m_G = 2000$ GeV, $\Gamma_G = 960$ GeV, $g_{R,u} = -g_{L,u} = -0.6g_S$, $g_{R,t} = -g_{L,t} = 4g_S$
 - (b) axigluon m2000w1000: $m_G = 2000$ GeV, $\Gamma_G = 1000$ GeV, $g_{R,u} = -0.8g_S$, $g_{R,t} = 6g_S$, $g_{L,i} = 0$

3. Z' model: This new gauge boson with flavor violating coupling contributes to the $q\bar{q} \rightarrow t\bar{t}$ process yielding a positive asymmetry if the decay width is large enough. The following parameters have been used to generate the sample of events:

(a) $z_{\text{prime}} \text{ m220}$: $m'_{Z'} = 220 \text{ GeV}$, $\Gamma_{Z'} = 2.9 \text{ GeV}$, $g_{Z'} = 0.7$

The $t\bar{t}$ forward-backward asymmetries values for the generated BSM samples are reported in Table 8.

Sample	B_1	B_2	C	$A_{\text{FB}}^{t\bar{t}}$
axigluon m2000w1000	-0.089(5)	0.097(5)	0.923(5)	0.037(2)
axigluon m2000w960	0.002(5)	0.016(5)	0.908(5)	0.073(2)
axigluon m200A4	-0.007(5)	0.014(5)	0.910(5)	0.125(2)
axigluon m200L5	0.133(5)	-0.119(5)	0.935(5)	0.047(2)
axigluon m200R5	-0.145(5)	0.156(5)	0.925(5)	0.050(2)
zprime m220	0.141(5)	-0.136(5)	0.860(5)	0.126(2)

TABLE 8: Polarization parameters (B_1 , B_2), spin correlation term (C), and $t\bar{t}$ forward-backward asymmetry for axigluons and Z' samples at the partonic level. The B_1 , B_2 , and C terms are obtained from the differential distribution of lepton angles, $\frac{1}{\sigma} \frac{d^2\sigma}{d\cos\theta_a d\cos\theta_b} = \frac{1}{4} [1 + B_1 \cos\theta_a + B_2 \cos\theta_b - C \cos\theta_a \cos\theta_b]$, where the angles are defined in the “off-diagonal basis” (See Ref. [47] for details).

Each of the 6 different BSM MCs and the MC@NLO MC is used to create 8 pseudo-samples, by reweighting the $\Delta y_{t\bar{t}}$ distribution, in the same way as described in Sec. 6.1. For each of these seven MCs, we therefore consider 8 pseudo-samples plus the nominal sample. We obtain in total $7 \times (8 + 1) = 63$ different pseudo-samples, each corresponding to a different value of the raw measurement and of the true asymmetry. Fig. 6 shows the difference between the measured value $A_{\text{FB}}^{t\bar{t}} = \frac{A_{\text{raw}}^{t\bar{t}} - x_0}{\epsilon_{\text{calib}}}$ corrected for the SM nominal calibration of Sec. 6.2 and the true asymmetry, as a function of $A_{\text{raw}}^{t\bar{t}}$ for the 63 pseudo-samples. The largest deviation from the nominal measurement occurs for the axigluon_m200L5 sample and amounts to 5.1%.

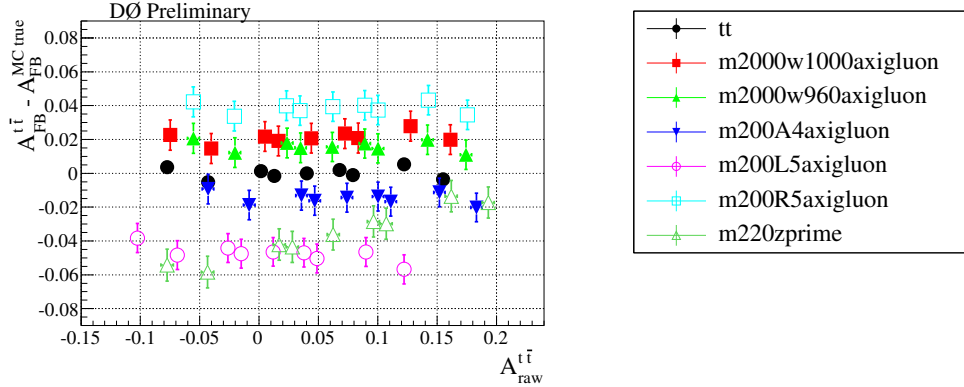


FIG. 6: For each of the pseudo-samples, difference between what would be measured using the nominal calibration curve obtained in Sec. 6.2 and the true $A_{\text{FB}}^{t\bar{t}}$, as a function of $A_{\text{raw}}^{t\bar{t}}$. The points labeled “tt” correspond to the MC@NLO pseudo-samples.

In Fig. 7 we present the results of a similar study but where the BSM samples have been reweighted to set the polarization of the top quark and antiquark to zero. For this study we define the polarization of the top quark and antiquark using the “off-diagonal basis” described for example in Ref. [47]. For completeness, the $t\bar{t}$ polarization of the benchmark models are given in Table 8. Note that, within the SM framework, the polarization is predicted to be negligible. Figure 7 shows that for the measured value of $A_{\text{raw}}^{t\bar{t}} = 11.3\%$, the maximal deviation relative to the SM calibration is reduced to 2% if we constrain the polarization to be null. Thus even if the polarization dependence is removed from consideration, some model dependence remains.

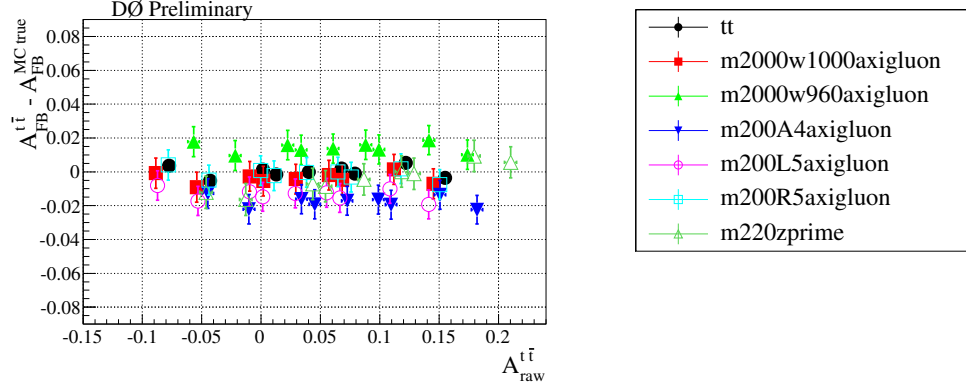


FIG. 7: For each of the pseudo-samples with zeroed polarization, difference between what would be measured using the nominal calibration curve obtained in Sec. 6.2 and the true $A_{\text{FB}}^{t\bar{t}}$, as a function of $A_{\text{raw}}^{t\bar{t}}$. The points labeled “tt” correspond to the MC@NLO pseudo-samples.

We conclude from these studies that the calibration of our $A_{\text{FB}}^{t\bar{t}}$ measurement is model dependent. In particular it depends upon the actual polarization of the top quark and antiquark. To obtain a model independent measurement, an additional systematic uncertainty of 5.1% has to be accounted for.

8. RESULT AND CONCLUSION

We have presented a measurement of the forward-backward asymmetry of the $t\bar{t}$ production in dilepton final states, using 9.7 fb^{-1} of proton-antiproton collisions at $\sqrt{s} = 1.96 \text{ TeV}$ with the DØ detector. The result, interpreted as a test of the validity of the Standard Model, is:

$$A_{\text{FB}}^{t\bar{t}} = 0.180 \pm 0.061 \text{ (stat)} \pm 0.032 \text{ (syst)} . \quad (13)$$

The NLO prediction for $A_{\text{FB}}^{t\bar{t}}$ is [1] $A_{\text{FB}}^{t\bar{t}} = 0.088 \pm 0.006$. Our measurement is compatible with the NLO prediction within 1.3 standard deviations. The DØ measurement performed in the lepton+jets channel [11] is $A_{\text{FB}}^{t\bar{t}} = 0.106 \pm 0.030$, which is compatible with our result at the level of 1.0 standard deviations.

To interpret the results as a model independent measurement of the asymmetry, an additional uncertainty arising from the possible range of top quark polarizations has to be accounted for, so that we obtain:

$$A_{\text{FB}}^{t\bar{t}} = 0.180 \pm 0.061 \text{ (stat)} \pm 0.032 \text{ (syst)} \pm 0.051 \text{ (model)} . \quad (14)$$

The summary of all measurements of $t\bar{t}$ asymmetry observables performed at the Tevatron is provided in Table 9. We also present the summary plot of $A_{\text{FB}}^{t\bar{t}}$ measurements at the Tevatron in Fig. 8.

Source	Asymmetry in %		
	$A_{\text{FB}}^{\ell\ell}$	A_{FB}^{ℓ}	$A_{\text{FB}}^{t\bar{t}}$
SM prediction	4.8 ± 0.4 [1]	3.8 ± 0.3 [1]	8.8 ± 0.6 [1]
CDF lepton+jets	–	9.4 ± 3.0 [6]	16.4 ± 4.7 [7]
CDF dilepton	7.6 ± 8.2 [8]	7.2 ± 6.0 [8]	42 ± 16 [9]
DØ lepton+jets	–	5.0 ± 3.6 [10]	10.6 ± 3.0 [11]
DØ dilepton	12.3 ± 5.6 [12]	4.4 ± 3.9 [12]	18.0 ± 6.9

TABLE 9: Summary of all measurements (including this analysis) of forward-backward asymmetry observables, performed at CDF and DØ, and comparison with the SM expectations.

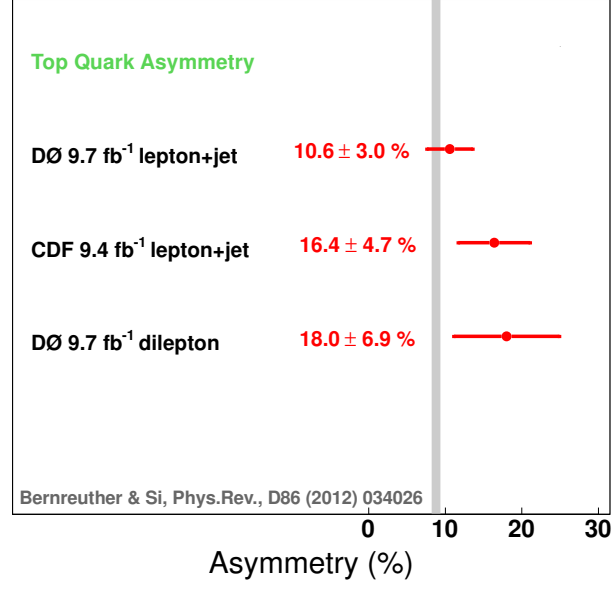


FIG. 8: Summary of $A_{\text{FB}}^{t\bar{t}}$ measurements (including this analysis) at the Tevatron. The CDF preliminary measurement in dilepton channel, $(42 \pm 16)\%$, is not shown in this plot.

-
- [1] W. Bernreuther and Z.-G. Si, Phys. Rev. D **86**, 034026 (2012), arXiv:1205.6580, we report only the scale uncertainties as uncertainties on the asymmetry predictions, which is known to be an aggressive approach.
 - [2] P. H. Frampton and S. L. Glashow, Phys. Lett. B **190**, 157 (1987).
 - [3] L. J. Hall and A. E. Nelson, Phys. Lett. B **153** (1985).
 - [4] O. Antunano, J. H. Kuhn, and G. Rodrigo, Phys. Rev. D **77** (2008), arXiv:0709.1652.
 - [5] P. H. Frampton, J. Shu, and K. Wang, Phys. Lett. B **683**, 294 (2010), 0911.2955.
 - [6] T. A. Aaltonen et al. (CDF Collaboration), Phys. Rev. D **88**, 072003 (2013), arXiv:1308.1120.
 - [7] T. Aaltonen et al. (CDF Collaboration), Phys. Rev. D **87**, 092002 (2013), arXiv:1211.1003.
 - [8] T. A. Aaltonen et al. (CDF Collaboration), Phys. Rev. Lett. **113**, 042001 (2014), arXiv:1404.3698.
 - [9] The CDF Collaboration (2011), CDF note 10436.
 - [10] V. M. Abazov et al. (D0 Collaboration), Accepted by Phys. Rev. D (2014), arXiv:1403.1294.
 - [11] V. M. Abazov et al. (D0 Collaboration), Submitted to Phys. Rev. D (2014), arXiv:1405.0421.
 - [12] V. M. Abazov et al. (D0 Collaboration), Phys. Rev. D **88**, 112002 (2013), arXiv:1308.6690.
 - [13] V. M. Abazov et al. (D0 Collaboration), Phys. Rev. Lett. **107**, 082004 (2011), arXiv:1105.0320.
 - [14] V. M. Abazov et al. (D0 Collaboration), Phys. Rev. Lett. **113**, 032002 (2014), arXiv:1405.1756.
 - [15] S. Abachi et al. (D0 Collaboration), Nucl. Instrum. Methods Phys. Res. A **338**, 185 (1994).
 - [16] V. M. Abazov et al. (D0 Collaboration), Nucl. Instrum. Methods Phys. Res. A **565**, 463 (2006), physics/0507191.
 - [17] M. Abolins et al., Nucl. Instrum. Methods Phys. Res. A **584**, 75 (2008), arXiv:0709.3750.
 - [18] R. Angstadt et al. (D0 Collaboration), Nucl. Instrum. Methods Phys. Res. A **622**, 298 (2010), arXiv:0911.2522.
 - [19] V. M. Abazov et al. (D0 Collaboration), Nucl. Instrum. Meth. A **750**, 78 (2014), arXiv:1401.0029.
 - [20] V. M. Abazov et al. (D0 Collaboration), Nucl. Instrum. Meth. A **737**, 281 (2014), arXiv:1307.5202.
 - [21] G. C. Blazey et al., hep-ex/0005012 (2000).
 - [22] V. M. Abazov et al. (D0 Collaboration), Nucl. Instrum. Meth. A **763**, 442 (2014), arXiv:1312.6873.
 - [23] A. Schwartzman, Fermilab-Thesis-2004-21 (2004).
 - [24] V. M. Abazov et al. (D0 Collaboration), Nucl. Instrum. Meth. A **763**, 290 (2014), arXiv:1312.7623.
 - [25] R. Brun and F. Carminati, CERN Program Library Long Writeup W5013 (1993) (unpublished).
 - [26] S. Frixione and B. R. Webber, JHEP **06**, 029 (2002), hep-ph/0204244.
 - [27] S. Frixione and B. R. Webber (2008), arXiv:0812.0770.
 - [28] G. Corcella et al., JHEP **01**, 010 (2001), hep-ph/0011363.
 - [29] P. M. Nadolsky et al., Phys. Rev. D **78**, 013004 (2008).
 - [30] S. Moch and P. Uwer, Phys. Rev. D **78**, 034003 (2008), arXiv:0804.1476.
 - [31] M. L. Mangano, M. Moretti, F. Piccinini, R. Pittau, and A. D. Polosa, JHEP **07**, 001 (2003), hep-ph/0206293.
 - [32] T. Sjostrand, S. Mrenna, and P. Z. Skands, J. High Energy Phys. **05** (2006), 026.
 - [33] R. Gavin, Y. Li, F. Petriello, and S. Quackenbush, Comput. Phys. Commun. **182**, 2388 (2011), arXiv:1011.3540.
 - [34] V. Abazov et al. (D0 Collaboration), Phys.Rev.Lett. **100**, 102002 (2008), arXiv:0712.0803.
 - [35] J. M. Campbell and R. Ellis (2012), <http://mcfm.fnal.gov>.
 - [36] V. Abazov et al. (D0 Collaboration), Phys. Rev. D **76**, 092007 (2007), arXiv:0705.2788.
 - [37] A. Grohsjean, Fermilab-Thesis-2008-92 (2008).
 - [38] G. Lepage, J. Chem. Phys. **27**, 192 (1978).
 - [39] G. Lepage, Cornell preprint CLNS:80-447 (1980).
 - [40] M. Galassi et al., *GNU Scientific Library Reference Manual* (Network Theory Ltd., 2009), 3rd ed., ISBN 0954161734, URL <http://www.gnu.org/software/gsl/>.
 - [41] Z. Hong, R. Edgar, S. Henry, D. Toback, J. S. Wilson, et al. (2014), arXiv:1403.7565.
 - [42] P. Skands, B. Webber, and J. Winter, JHEP **1207**, 151 (2012), arXiv:1205.1466.
 - [43] J. Winter, P. Z. Skands, and B. R. Webber, EPJ Web Conf. **49**, 17001 (2013), arXiv:1302.3164.
 - [44] A. Carmona, M. Chala, A. Falkowski, S. Khatibi, M. M. Najafabadi, et al. (2014), arXiv:1401.2443.
 - [45] M. S. Carena, A. Daleo, B. A. Dobrescu, and T. M. Tait, Phys. Rev. D **70**, 093009 (2004), hep-ph/0408098.
 - [46] J. Alwall, R. Frederix, S. Frixione, V. Hirschi, F. Maltoni, et al. (2014), arXiv:1405.0301.
 - [47] W. Bernreuther, J.Phys. **G35**, 083001 (2008), arXiv:0805.1333.